FLEXURAL WAVE FILTERING AND PLATONIC POLARISERS IN THIN ELASTIC PLATES

by M. J. A. SMITH[†]

(*Department of Mathematics, The University of Auckland, Private Bag* 92019*, Auckland* 1142*, New Zealand*)

M. H. MEYLAN

(*School of Mathematical and Physical Sciences, The University of Newcastle, New South Wales* 2308*, Newcastle, Australia*)

and

R. C. McPHEDRAN

(*CUDOS ARC Centre of Excellence, School of Physics, University of Sydney, New South Wales* 2006*, Sydney, Australia*)

[Received 5 February 2013. Revise 6 June 2013. Accepted 9 June 2013]

Summary

A solution method is given to the problem of plane wave propagation through one- and two-dimensional platonic arrays. The problem is formulated in terms of boundary integral equations and a solution is constructed using boundary element methods. Previous work has been restricted to simple geometries such as circles, pins and squares, and here the framework is extended to consider scatterers of arbitrary shape subject to clamped-edge boundary conditions at the edge. This is done by constructing scattering matrices for a single grating and using Bloch's theorem to form an eigenvalue problem which connects the grating problem to the array problem. The associated eigenvalues then permit the construction of band surfaces which reveal the flexural wave filtering capabilities of different geometries, as well as the behaviour of Bloch waves within the array. Multiple geometries are investigated and the first band surfaces are computed for these specific cases.

1. Introduction

Regularly arranged structures which guide and disperse wave energy are important tools with wide applications in science and engineering. These range from the design of spectrometers (**1**), to the construction of floating offshore wave energy generators (**2**), the control of sound waves by arrays of trees (**3**) and are even used to determine the behaviour of ice floes in the marginal ice zone (**4**). They are also especially relevant in the study of photonic crystals, phononic crystals, plasmonic crystals (that is (**5–7**)) and most recently, platonic crystals (**8–12**), which are considered here.

Platonic crystals (PlaCs) are defined as periodic structures which guide the propagation of flexural, or bending, waves through thin elastic plates (**13**). Here we investigate elastic wave propagation through an infinite stack of platonic gratings which are constructed using scatterers of arbitrary

[†]<m.smith@math.auckland.ac.nz>

Q. Jl Mech. Appl. Math, Vol. 0. No. 0 © The Author, 2013. Published by Oxford University Press;

Advance Access publication xxx 2013. doi:10.1093/qjmam/hbt013

geometry (note that the term platonic refers to any structure embedded in a thin plate, and that a grating is defined as a one-dimensional array). Previously, the bulk of the research into platonic structures has considered only circular scatterers (**8**, **9**) and pins (**14–16**) using multipole techniques, or square cavities (**11**) using finite element models. Here the solution is obtained using boundary integral equations, in an extension to previous work by the authors on single arbitrary scatterers and finite clusters of pins (**15**, **17**, **18**). Other examples of platonic crystals that have received considerable attention include plates that possess substructures, such as arrays of line stiffeners, and arrays of line attachments (**19–23**).

In contrast to the Helmholtz equation which governs most wave propagation (for example, in acoustics and electromagnetic theory), platonic crystals are governed by the fourth-order biharmonic equation. It can be shown straightforwardly that the biharmonic operator decomposes into a product of Helmholtz and modified Helmholtz operators. The presence of this additional modified Helmholtz operator gives rise to an additional evanescent wave field component to the solution, which in certain cases permits strong trapping behaviours inside these periodic structures compared to the Helmholtz equation alone (**15**). In fact, the presence of evanescent modes have also been shown to assist with coupling to slow light across waveguides in photonics (**24**). It is possible to restrict the solution outline here for the biharmonic equation and consider the associated problem for the Helmholtz equation from inspection, due to the linearity present in both our operator and boundary conditions. However, we should note that integral representations for the problem of both a single scatterer and a periodic array, governed by the Helmholtz equation, have also been investigated previously (**25**, **26**).

To demonstrate the behaviour of flexural waves inside the PlaC we will construct band surfaces for a number of different geometries. These band surfaces are a useful visual tool for determining the group velocity inside a PlaC and reveal the incident frequencies and angles where wave propagation through an array is possible. These different geometries can alter the curvature of band surfaces and can therefore filter incident waves in very different ways. For simplicity, we consider only cavities with clamped boundary conditions, which have been shown by Poulton *et al.* (**10**) and Movchan *et al.* (**9**) to have flat band surfaces and large band gaps, relative to the surfaces associated with free-edge boundary conditions.

For the problem of a single grating one can use Green's second identity to form a system of boundary integral equations to determine the unknown displacements and normal derivatives at the edge of the central scatterer. These can then be solved using boundary element methods. It is also possible to obtain the solution to the arbitrary shape problem using finite element methods, as demonstrated in Farhat *et al.* (**11**) and Dossou *et al.* (**27**), however there are circumstances where the boundary element method (BEM) is the preferred approach, for example, at high wave number values. That said, the direct representation of the quasi-periodic Green's function is poorly convergent and requires suitable acceleration. A comparison of the various methods used to evaluate the quasi-periodic Green's function for the Helmholtz equation (away from Wood anomalies—see below) is given in Linton (**28**), along with tables of values which can be used for numerical validation. The relationship between the quasi-periodic Green's function for a single grating and a doubly periodic array of scatterers is given in McPhedran *et al.* (**29**), which also has useful tables of values.

The phenomenon of Wood anomalies, or grating resonances, is well-known and was first experimentally observed by Wood (**30**) and explained theoretically by Lord Rayleigh (**31**). They correspond to the excitation of a propagating order which travels along the grating, rapidly decaying in any direction away from the interface, but ultimately propagating to infinity parallel to the interface (**32**). They result in the quasi-periodic Green's function for the grating becoming singular, irrespective of the representation used. There is ongoing research on the effective evaluation of the quasi-periodic

Green's function in the vicinity of these Wood anomalies, including recent work by Barnett and Greengard (**26**), who use contour deformation, and Bruno and Delourme (**33**) who propose using modified Green's functions. For our purposes, when constructing band surfaces we simply remove points that correspond to Wood anomalies from our calculations and use interpolation to reconstruct any missing segments of the band surface.

Note that when using boundary integral methods for the case of a single scatterer, we encounter the problem of irregular frequencies (**17**). These irregular frequencies correspond to an adjoint interior problem whose boundary conditions are unknown and are completely non-physical. For the case of a single scatterer we have a clear interior and exterior domain, however for any array of scatterers, irregular frequencies are not present as there is no finite interior domain.

The band surfaces themselves are constructed using the procedure outlined in Botten *et al.* (**34**). That is, once the solution around the edge of the central scatterer is known, we construct the reflection and transmission matrices for a single grating, as discussed in Movchan *et al.* (**8**). Once the reflection and transmission matrices for a single grating have been calculated, the extension to the problem of a doubly periodic array reduces to that of a generalised eigenvalue problem as these matrices completely characterise the Bloch waves that can propagate through an array to infinity (**34**).

For the particular case of circular or pinned scatterers, it is possible to obtain multipole solutions and subsequently the reflection and transmission coefficients can be written as closed-form expressions (**8**). From this, one can then follow the scattering matrix approach here to construct the associated band surfaces. Alternatively, the dispersion relation for the plate can be written in terms of lattice sums (**9**, **15**) or trigonometric functions (**35**) and solved directly to obtain the band surfaces.

A number of geometries are investigated, and we find that large aspect ratios (that is, long, slender scatterers) are associated with highly anisotropic behaviour as well as preferential directions of propagation along the x- and y-axis for different wave number intervals. Such structures are referred to here as platonic polarisers and have been identified for the first time here. We are also able to demonstrate the existence of ultraflat bands, which are defined as band surfaces that feature near-zero curvature. Such surfaces give rise to low group velocities and are connected with the concepts of slow and frozen light in photonics (**36**, **37**). Such ultra low group velocities can lead to large delays in signal propagation through arrays, which may prove useful in network buffering and other device applications (for example, in enhanced nonlinear platonic crystals). Other features of these band surfaces include intervals of negative refraction, and wide band gaps above and below the first surface.

The outline of the article is as follows. In Section 2, we provide a problem outline and introduce the quasi-periodic Green's functions for the Helmholtz and modified Helmholtz operators. In Section 3, we present the boundary element solution for clamped-edge boundary conditions which allows us to retrieve the solution at the edge of the central scatterer. In Section 4, representations for the quasi-periodic Green's functions are given in terms of grating sums, and attention is paid to the acceleration of the associated Scholmilch series. In Section 5, we compute the reflection and transmission coefficients necessary to construct the associated matrices for the case of a single grating. In Section 6, the conservation of energy relation calculated in Movchan *et al.* (**8**) for a platonic grating is shown in matrix form. In Section 7, we outline the procedure for constructing the band surface of a two-dimensional square array in terms of the reflection and transmission matrices for a single grating. This is followed in Section 8 by a survey of first band surfaces for a number of different geometries, the energy reflection and transmission by a single grating for a number of geometries, and an investigation into the existence of a perfectly flat band for the case of an elliptical scatter.

The Appendix section presents the solution for the specific case of a circular scatterer for comparison and additional numerical validation.

2. Problem formulation

We begin with the biharmonic plate equation in the frequency domain which is given by

$$(\Delta^2 - k^4)w = (\Delta + k^2)(\Delta - k^2)w = 0, \tag{2.1}$$

where w is the plate displacement, $k^2 = \omega\sqrt{\rho h/D}$, ω is the angular frequency, ρ is the mass density, h is the thickness and D is the flexural rigidity of the plate. Here we have assumed a time dependence of $e^{-\mathrm{i}\omega t}$.

As the biharmonic equation is linear and decomposes into a product of Helmholtz and modified Helmholtz operators, we can accordingly decompose the displacement as follows:

$$w = w_{\mathrm{I}}^{\mathrm{H}} + w_{\mathrm{S}}^{\mathrm{H}} + w_{\mathrm{I}}^{\mathrm{M}} + w_{\mathrm{S}}^{\mathrm{M}}. \tag{2.2}$$

We consider here incident plane waves of the form:

$$w_{\mathrm{I}}^{\mathrm{H}} = \frac{\delta_0}{\sqrt{|\chi_0|}} e^{\mathrm{i}\alpha_0 x - \mathrm{i}\chi_0 y}, \tag{2.3a}$$

$$w_{\mathrm{I}}^{\mathrm{M}} = \frac{\widehat{\delta}_0}{\sqrt{|\widehat{\chi}_0|}} e^{\mathrm{i}\alpha_0 x - \mathrm{i}\hat{\chi}_0 y}, \tag{2.3b}$$

where δ_0 denotes the amplitude of a Helmholtz incident wave, $\widehat{\delta}_0$ denotes the amplitude of a modified Helmholtz incident wave, $\alpha_0 = k\sin\theta_i$, $\chi_0 = k\cos\theta_i$, θ_i is the incident angle, and $\alpha_0^2 + \hat{\chi}_0^2 = -k^2$ (that is $\hat{\chi}_0 = \mathrm{i}\tau_0$, where $\tau_0 > 0$). Note that the incident potentials above have inverse square root amplitude prefactors. These are introduced so that our conservation of energy relation (6.1) is appropriately normalised. Furthermore, we consider only one incident wave type at a given time (for example, $\delta_0 = 1$ and $\widehat{\delta}_0 = 0$).

We now construct the boundary equations for a platonic grating comprised of identically spaced scatterers of arbitrary geometry. If the scatterers are circular, the solution can be found using multipole techniques (see the Appendix section). Using Green's second identity in a manner similar to Smith *et al.* (**17**), the plate displacement can be expressed by the following system of boundary integral equations:

$$\tfrac{1}{2}w^{\mathrm{M}}(\mathbf{x}) = w_{\mathrm{I}}^{\mathrm{M}}(\mathbf{x}) + \sum_{m=-\infty}^{\infty} \int_{\partial\Omega_m} \left\{ \partial_{n'} G^{\mathrm{M}}(\mathbf{x}, \mathbf{x}') w^{\mathrm{M}}(\mathbf{x}') - \partial_{n'} w^{\mathrm{M}}(\mathbf{x}') G^{\mathrm{M}}(\mathbf{x}, \mathbf{x}') \right\} dS', \tag{2.4a}$$

$$\tfrac{1}{2}w^{\mathrm{H}}(\mathbf{x}) = w_{\mathrm{I}}^{\mathrm{H}}(\mathbf{x}) + \sum_{m=-\infty}^{\infty} \int_{\partial\Omega_m} \left\{ \partial_{n'} G^{\mathrm{H}}(\mathbf{x}, \mathbf{x}') w^{\mathrm{H}}(\mathbf{x}') - \partial_{n'} w^{\mathrm{H}}(\mathbf{x}') G^{\mathrm{H}}(\mathbf{x}, \mathbf{x}') \right\} dS', \tag{2.4b}$$

for all $\mathbf{x} \in \partial\Omega_m$ where $m \in \mathbb{Z}$. Here $G^{\mathrm{H}}(\mathbf{x}, \mathbf{x}') = \mathrm{i}/4H_0^{(1)}(kr)$ and $G^{\mathrm{M}}(\mathbf{x}, \mathbf{x}') = \mathrm{i}/4H_0^{(1)}(\mathrm{i}kr)$ denote the Green's functions for the Helmholtz and modified Helmholtz equations, respectively, which are

expressed in terms of zero-order Hankel functions, with $r = |\mathbf{x} - \mathbf{x}'|$ denoting the distance between the field and source points, respectively. The normal derivatives are defined as $\partial_{n'} = (\partial_{x'}, \partial_{y'}) \cdot \mathbf{n}'$ where $\mathbf{n}'$ is the normal unit vector to the boundary, pointing outwards. We denote the boundary of the mth smooth cavity in our infinite array by $\partial\Omega_m$.

As the grating is regularly structured, the variation in the displacement between adjacent bodies can be represented by the quasi-periodicity condition:

$$w(\mathbf{x}' + (md, 0)) = w(\mathbf{x}'_m) = e^{\mathrm{i}\alpha_0 md} w(\mathbf{x}'), \tag{2.5}$$

where d denotes the period of the grating. Additionally the field point can be restricted to the central scatterer, and consequently (2.4a) and (2.4b) can be represented by the more compact system

$$\tfrac{1}{2} w^{\mathrm{M}}(\mathbf{x}) = w^{\mathrm{M}}_{\mathrm{I}}(\mathbf{x}) + \int_{\partial\Omega_0} \left\{ \partial_{n'} G^{\mathrm{M}}_g(\mathbf{x}, \mathbf{x}')\, w^{\mathrm{M}}(\mathbf{x}') - \partial_{n'} w^{\mathrm{M}}(\mathbf{x}')\, G^{\mathrm{M}}_g(\mathbf{x}, \mathbf{x}') \right\} dS', \tag{2.6a}$$

$$\tfrac{1}{2} w^{\mathrm{H}}(\mathbf{x}) = w^{\mathrm{H}}_{\mathrm{I}}(\mathbf{x}) + \int_{\partial\Omega_0} \left\{ \partial_{n'} G^{\mathrm{H}}_g(\mathbf{x}, \mathbf{x}')\, w^{\mathrm{H}}(\mathbf{x}') - \partial_{n'} w^{\mathrm{H}}(\mathbf{x}')\, G^{\mathrm{H}}_g(\mathbf{x}, \mathbf{x}') \right\} dS', \tag{2.6b}$$

for $\mathbf{x} \in \partial\Omega_0$, where we have the quasi-periodic Green's functions

$$G^{\mathrm{H}}_g(\mathbf{x}, \mathbf{x}') = \sum_{m=-\infty}^{\infty} G^{\mathrm{H}}(\mathbf{x}, \mathbf{x}'_m) e^{\mathrm{i}\alpha_0 md}, \tag{2.7a}$$

$$\partial_{n'} G^{\mathrm{H}}_g(\mathbf{x}, \mathbf{x}') = \sum_{m=-\infty}^{\infty} \partial_{n'} G^{\mathrm{H}}(\mathbf{x}, \mathbf{x}'_m) e^{\mathrm{i}\alpha_0 md}, \tag{2.7b}$$

$$G^{\mathrm{M}}_g(\mathbf{x}, \mathbf{x}') = \sum_{m=-\infty}^{\infty} G^{\mathrm{M}}(\mathbf{x}, \mathbf{x}'_m) e^{\mathrm{i}\alpha_0 md}, \tag{2.7c}$$

$$\partial_{n'} G^{\mathrm{M}}_g(\mathbf{x}, \mathbf{x}') = \sum_{m=-\infty}^{\infty} \partial_{n'} G^{\mathrm{M}}(\mathbf{x}, \mathbf{x}'_m) e^{\mathrm{i}\alpha_0 md}. \tag{2.7d}$$

Here the subscript g is introduced to represent a Green's function for a grating as opposed to a conventional Green's function. We consider the simplest possible condition that can be imposed on a thin plate—when the edges of the perforations are clamped.

3. Clamped-edge boundary conditions

For thin plates the boundary conditions for a scatterer with clamped-edge conditions are given by

$$w(\mathbf{x}') = 0, \quad \text{and} \quad \partial_{n'} w(\mathbf{x}') = 0, \quad \text{for} \quad \mathbf{x}' \in \partial\Omega_0. \tag{3.1}$$

This implies that

$$w^{\mathrm{H}} = -w^{\mathrm{M}}, \tag{3.2a}$$

$$\partial_{n'} w^{\mathrm{H}} = -\partial_{n'} w^{\mathrm{M}}, \tag{3.2b}$$

which provides the necessary coupling condition to solve the system (2.6a) and (2.6b) via some numerical scheme, such as BEM. Such methods begin by subdividing the boundary of the scatterer

into q panels (with each panel denoted by $\partial\Omega_{0q}$) of approximately constant length over which the associated displacement and normal derivative is assumed constant. This admits the block-matrix system:

$$\mathbf{Mz} = \left[\begin{array}{c|c} \frac{1}{2}\mathbf{I} - \mathbf{A}^{\mathrm{M}} & \mathbf{B}^{\mathrm{M}} \\ \hline \frac{1}{2}\mathbf{I} - \mathbf{A}^{\mathrm{H}} & \mathbf{B}^{\mathrm{H}} \end{array}\right] \left[\begin{array}{c} \boldsymbol{\xi} \\ \boldsymbol{\eta} \end{array}\right] = \mathbf{f}, \tag{3.3}$$

where $\boldsymbol{\xi}_p = w^{\mathrm{H}}(\overline{\mathbf{x}}_p)$, $\boldsymbol{\eta}_p = \partial_{n'} w^{\mathrm{H}}(\overline{\mathbf{x}}_p)$,

$$\mathbf{A}^{\mathrm{H,M}}_{pq} = \int_{\partial\Omega_{0q}} \partial_{n'} G^{\mathrm{M,H}}_g(\overline{\mathbf{x}}_p, \mathbf{x}')dS', \tag{3.4a}$$

$$\mathbf{B}^{\mathrm{H,M}}_{pq} = \int_{\partial\Omega_{0q}} G^{\mathrm{M,H}}_g(\overline{\mathbf{x}}_p, \mathbf{x}')dS', \tag{3.4b}$$

and $\mathbf{f} = [\mathbf{0}, \boldsymbol{\xi}^i]^{\mathrm{T}}$ or $\mathbf{f} = [\boldsymbol{\eta}^i, \mathbf{0}]^{\mathrm{T}}$ depending on the choice of the incident wave potential. Here $\boldsymbol{\xi}^i_p = w^{\mathrm{H}}_{\mathrm{I}}(\overline{\mathbf{x}}_p)$, $\boldsymbol{\eta}^i_p = -w^{\mathrm{M}}_{\mathrm{I}}(\overline{\mathbf{x}}_p)$, $\mathbf{I}$ denotes the identity matrix and $\overline{\mathbf{x}}_p$ denotes the midpoint of the pth panel.

Note that the quasi-periodic Green's functions (2.7) above are singular at $r \equiv 0$. Numerically we overcome this by adding and subtracting the log singularity that is encountered by the zero-order Hankel functions as $kr \to 0$ in a procedure known as the singularity subtraction method (**38**). In contrast, the normal derivatives of these Green's functions are smooth across $r \equiv 0$ and so interpolation is used to recover values at $r \equiv 0$ when constructing the $\mathbf{A}$ and $\mathbf{B}$ matrices.

Furthermore, the Green's function for the Helmholtz equation is well-known to have slow convergence and needs to be accelerated by an efficient numerical scheme. This is the topic of the following section.

4. Acceleration of the Green functions

The technique outlined below is from Nicorovici and McPhedran (**39**) and is included here for completeness. We begin by considering the function:

$$\begin{aligned} G^{\mathrm{H}}_g(\mathbf{x}, \mathbf{x}') &= \sum_{m=-\infty}^{\infty} G^{\mathrm{H}}(\mathbf{x}, \mathbf{x}'_m) e^{\mathrm{i}\alpha_0 md} \\ &= \frac{\mathrm{i}}{4} \sum_{m=-\infty}^{\infty} H^{(1)}_0\left(k\sqrt{(x - x' - md)^2 + (y - y')^2}\right) e^{\mathrm{i}\alpha_0 md}. \end{aligned} \tag{4.1}$$

The expression (4.1) can be rewritten using Graf's addition theorem

$$C_\nu(w)e^{\mathrm{i}\nu\chi} = \sum_{l=-\infty}^{\infty} C_{l+\nu}(u)J_l(\nu)e^{\mathrm{i}l\alpha}, \quad \text{where} \quad |ve^{\mathrm{i}\alpha}| < |u|, \tag{4.2}$$

(formula (9·1·79) in Abramowitz and Stegun (**40**)) within the fundamental cell $(x, y) = [-d/2, d/2] \times [-d/2, d/2]$, where C_ν denotes an arbitrary Bessel function. Here the lines u, v

and w form a closed triangle with $w = \sqrt{u^2 + v^2 - 2uv\cos\alpha}$, α denoting the angle between the lines u and v, and χ denoting the angle between the lines u and w. This admits the representation

$$G_g^{\mathrm{H}}(\mathbf{x}, \mathbf{x}') = \frac{\mathrm{i}}{4}\left[H_0^{(1)}(kr) + S_0^{\mathrm{H,G}} J_0(kr) + 2\sum_{l=1}^{\infty} S_l^{\mathrm{H,G}} J_l(kr)\cos(l\theta)\right], \tag{4.3}$$

where we introduce the grating sum

$$S_l^{\mathrm{H,G}}(\alpha_0, k, d) = \sum_{n\neq 0} H_l^{(1)}(|n|kd) e^{\mathrm{i}\alpha_0 nd} e^{\mathrm{i}l\varphi_n}. \tag{4.4a}$$

Here $\varphi_n = \pi H(-n)$, $H(x)$ denotes a Heaviside function, and (r, θ) are polar coordinates with $r = \sqrt{(x-x')^2 + (y-y')^2}$ and $\theta = \tan^{-1}((y-y')/(x-x'))$. The grating sum $S_l^{\mathrm{H,G}}$ in (4.4a) has a radius of convergence $r = d$, and can be decomposed straightforwardly into even and odd index grating sums:

$$S_{2l}^{\mathrm{H,G}}(\alpha_0, k, d) = 2\sum_{n=1}^{\infty} H_{2l}^{(1)}(nkd)\cos(\alpha_0 nd), \tag{4.5a}$$

$$S_{2l-1}^{\mathrm{H,G}}(\alpha_0, k, d) = 2\mathrm{i}\sum_{n=1}^{\infty} H_{2l-1}^{(1)}(nkd)\sin(\alpha_0 nd). \tag{4.5b}$$

Series of this type are known as Schlomilch series and are notorious for poor convergence (**41**). Directly convergent expressions for these Schlomilch series can be found in Twersky (**41**), however we include below (2.49), (2.53) and (2.54) from Linton (**28**) which are the result of applying Kummer's method to the expressions in (**41**):

$$S_0^{\mathrm{H,G}} = -1 - \frac{2\mathrm{i}}{\pi}\left[\gamma + \log\left(\frac{kd}{4\pi}\right)\right] + \frac{2}{\chi_0 d} - \frac{\mathrm{i}d^2(k^2 + 2\alpha_0^2)}{4\pi^3}\zeta(3) - \frac{2\mathrm{i}}{d}\sum_{m\in\mathbb{Z}\setminus\{0\}}\left(\frac{\mathrm{i}}{\chi_m} - \frac{d}{2\pi|m|} - \frac{d^3(k^2 + 2\alpha_0^2)}{16\pi^3|m|^3}\right), \tag{4.6a}$$

$$S_{2l}^{\mathrm{H,G}} = \frac{2e^{-2\mathrm{i}l\theta_0}}{\chi_0 d} + 2\sum_{m=1}^{\infty}\left\{\frac{e^{-2\mathrm{i}l\theta_m}}{\chi_m d} + \frac{e^{2\mathrm{i}l\theta_{-m}}}{\chi_{-m}d} + \frac{\mathrm{i}(-1)^l}{m\pi}\left(\frac{kd}{4m\pi}\right)^{2l}\right\} - \frac{2\mathrm{i}(-1)^l}{\pi}\left(\frac{kd}{4\pi}\right)^{2l}\zeta(2l+1) + \frac{\mathrm{i}}{l\pi} + \frac{\mathrm{i}}{\pi}\sum_{m=1}^{l}\frac{(-1)^m 2^{2m}(l+m-1)!}{(2m)!(l-m)!}\left(\frac{2\pi}{dk}\right)^{2m} B_{2m}\left(\frac{\alpha_0 d}{2\pi}\right), \tag{4.6b}$$

$$S_{2l-1}^{\mathrm{H,G}} = -\frac{2e^{-\mathrm{i}(2l-1)\theta_0}}{\chi_0 d} - 2\sum_{m=1}^{\infty}\left\{\frac{e^{-\mathrm{i}(2l-1)\theta_m}}{\chi_m d} + \frac{e^{\mathrm{i}(2l-1)\theta_{-m}}}{\chi_{-m} d} + \frac{\alpha_0 d(-1)^l l}{m^2\pi^2}\left(\frac{kd}{4m\pi}\right)^{2l-1}\right\}$$
$$- \frac{2\alpha_0 d(-1)^l l}{\pi^2}\left(\frac{kd}{4\pi}\right)^{2l-1}\zeta(2l+1)$$
$$- \frac{2}{\pi}\sum_{m=0}^{l-1}\frac{(-1)^m 2^{2m}(l+m-1)!}{(2m+1)!(l-m-1)!}\left(\frac{2\pi}{dk}\right)^{2m+1} B_{2m+1}\left(\frac{\alpha_0 d}{2\pi}\right), \quad (4.6c)$$

where $\zeta(z)$ represents the Riemann zeta function, γ denotes the Euler–Mascheroni constant, $B_n(z)$ represents a Bernoulli polynomial of order n,

$$\alpha_n = k\sin(\theta_n) = \alpha_0 + \frac{2\pi n}{d}, \qquad \text{and} \qquad \chi_n = \begin{cases}\sqrt{k^2-\alpha_n^2}, & \alpha_n^2 \le k^2\\ \mathrm{i}\sqrt{\alpha_n^2-k^2}, & \alpha_n^2 > k^2.\end{cases} \quad (4.7)$$

The derivatives of the Green's function above are given by

$$\partial_{\xi'} G_g^{\mathrm{H}} = -\frac{\mathrm{i}k}{4}\left[H_1^{(1)}(kr)\partial_{\xi'} r + S_0^{\mathrm{H,G}} J_1(kr)\partial_{\xi'} r\right.$$
$$\left. + \sum_{l=1}^{\infty} S_l^{\mathrm{H,G}}\left\{\left(J_{l+1}(kr) - J_{l-1}(kr)\right)\partial_{\xi'} r\cos(l\theta) + \frac{2l}{k}J_l(kr)\sin(l\theta)\partial_{\xi'}\theta\right\}\right], \quad (4.8)$$

where $\xi' = x'$ or $\xi' = y'$ as required to compute $\partial_{n'} G_g^{\mathrm{H}}$.

In general, the Green's function representations (2.7c) and (2.7d) for the modified Helmholtz equation G_g^{M} can be computed straightforwardly as the summand decays exponentially for $|m| \to \infty$. However, for consistency one can express the quasi-periodic Green's function for the modified Helmholtz case as

$$G_g^{\mathrm{M}}(\mathbf{x},\mathbf{x}') = \frac{1}{2\pi}\left[K_0(kr) + S_0^{\mathrm{K,G}} I_0(kr) + 2\sum_{l=1}^{\infty} S_l^{\mathrm{K,G}} I_l(kr)\cos(l\theta)\right], \quad (4.9)$$

where

$$S_l^{\mathrm{K,G}} = \sum_{n\neq 0} K_l(|n|kd)e^{\mathrm{i}\alpha_0 nd}e^{\mathrm{i}l\varphi_n}, \quad (4.10)$$

or after decomposition into even and odd orders,

$$S_{2l}^{\mathrm{K,G}} = 2\sum_{n=1}^{\infty} K_{2l}(nkd)\cos(\alpha_0 nd), \quad (4.11a)$$

$$S_{2l-1}^{\mathrm{K,G}} = 2\mathrm{i}\sum_{n=1}^{\infty} K_{2l-1}(nkd)\sin(\alpha_0 nd). \quad (4.11b)$$

The grating sums for the modified Helmholtz equation are in general, rapidly convergent and directly evaluable (**8**). The derivatives for the modified Green's function can be obtained via

$$\partial_{\xi'} G_g^{\mathrm{M}} = \frac{k}{2\pi}\left[-K_1^{(1)}(kr)\partial_{\xi'} r + S_0^{\mathrm{K,G}} I_1(kr)\partial_{\xi'} r + \sum_{l=1}^{\infty} S_l^{\mathrm{K,G}}\left\{\left(I_{l+1}(kr)+I_{l-1}(kr)\right)\partial_{\xi'} r\cos(l\theta) - \frac{2l}{k} I_l(kr)\sin(l\theta)\partial_{\xi'}\theta\right\}\right], \quad (4.12)$$

where ξ' is defined as above.

Care must be taken with the quasi-periodic Green's function for the Helmholtz equation as it fails to converge at particular combinations of k and α_0 which correspond to Wood anomalies (**30**, **31**). Wood anomalies occur when a diffraction order switches from being evanescent to propagating, that is when $\chi_m \equiv 0$ for some $m \in \mathbb{Z}$. It is also possible to have double Wood anomalies which correspond to $\alpha_m = -\alpha_n = k$ for some $m, n \in \mathbb{Z}$ and occur when $kd/2\pi \in \mathbb{Z}$ (**26**).

5. Reflection and transmission coefficients

We follow a similar procedure to the one outlined in Movchan *et al.* (**8**), except here we generalise for bodies of arbitrary shape. However it is first necessary to introduce appropriate notation in order to construct the reflection and transmission matrices for our platonic crystal.

In particular, we introduce the notation w^{HH} and w^{MH} to denote the w^{H} and w^{M} components of the displacement (respectively), when a Helmholtz incident wave $w_{\mathrm{I}}^{\mathrm{H}}$ is present. We also introduce w^{MM} and w^{HM} to denote w^{M} and w^{H} (respectively), for the modified Helmholtz incident wave $w_{\mathrm{I}}^{\mathrm{M}}$. That is, the second superscript refers to the incident wave type and the first refers to the displacement component. It is necessary to consider all these possible combinations as modified Helmholtz incident waves give rise to Helmholtz waves and vice versa.

We begin by applying Green's second identity around the central cell as shown in Fig. 1, using two special test functions along with the displacements w^{HH}, w^{HM}, w^{MH} and w^{MM}. The test functions

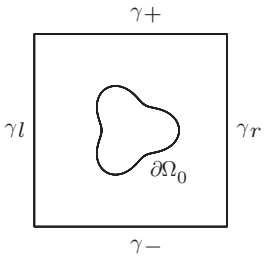

Fig. 1 An outline of the central cell for a square lattice containing an arbitrarily shaped scatterer

are defined as

$$v_m^{\mathrm{H}} = \frac{1}{\sqrt{|\mu_m|}} e^{-\mathrm{i}\alpha_m x + \mathrm{i}\mu_m y}, \tag{5.1a}$$

$$v_m^{\mathrm{M}} = \frac{1}{\sqrt{|\widehat{\mu}_m|}} e^{-\mathrm{i}\alpha_m x + \mathrm{i}\widehat{\mu}_m y}, \tag{5.1b}$$

where $\mu_m = \pm\chi_m$ and $\widehat{\mu}_m = \pm\widehat{\chi}_m$, which are specified later.

When a Helmholtz incident wave is considered the total wave field on the top of the fundamental cell ($\mathbf{x} \in \gamma_+$) can be expressed in plane wave form as

$$w = w_{\mathrm{I}}^{\mathrm{H}} + \sum_p \frac{R_p^{\mathrm{H}}}{\sqrt{|\chi_p|}} e^{\mathrm{i}\alpha_p x + \mathrm{i}\chi_p y} + \sum_p \frac{\widehat{R}_p^{\mathrm{H}}}{\sqrt{|\widehat{\chi}_p|}} e^{\mathrm{i}\alpha_p x + \mathrm{i}\widehat{\chi}_p y}, \tag{5.2a}$$

where R_p^{H} and $\widehat{R}_p^{\mathrm{H}}$ denote the reflection coefficients for the Helmholtz and modified Helmholtz fields, respectively. This can be decomposed in a similar manner into $w = w^{\mathrm{HH}} + w^{\mathrm{MH}}$ where

$$w^{\mathrm{HH}}(\mathbf{x}) = w_{\mathrm{I}}^{\mathrm{H}} + \sum_p \frac{R_p^{\mathrm{H}}}{\sqrt{|\chi_p|}} e^{\mathrm{i}\alpha_p x + \mathrm{i}\chi_p y}, \quad w^{\mathrm{MH}}(\mathbf{x}) = \sum_p \frac{\widehat{R}_p^{\mathrm{H}}}{\sqrt{|\widehat{\chi}_p|}} e^{\mathrm{i}\alpha_p x + \mathrm{i}\widehat{\chi}_p y}. \tag{5.2b}$$

Likewise for a modified incident wave the total field at the top of the cell is given by

$$w = w_{\mathrm{I}}^{\mathrm{M}} + \sum_p \frac{R_p^{\mathrm{M}}}{\sqrt{|\chi_p|}} e^{\mathrm{i}\alpha_p x + \mathrm{i}\chi_p y} + \sum_p \frac{\widehat{R}_p^{\mathrm{M}}}{\sqrt{|\widehat{\chi}_p|}} e^{\mathrm{i}\alpha_p x + \mathrm{i}\widehat{\chi}_p y}, \tag{5.3a}$$

where R_p^{M} and $\widehat{R}_p^{\mathrm{M}}$ denote the reflection coefficients for the Helmholtz and modified Helmholtz fields, respectively. This can be decomposed into $w = w^{\mathrm{HM}} + w^{\mathrm{MM}}$, where

$$w^{\mathrm{HM}}(\mathbf{x}) = \sum_p \frac{R_p^{\mathrm{M}}}{\sqrt{|\chi_p|}} e^{\mathrm{i}\alpha_p x + \mathrm{i}\chi_p y}, \quad w^{\mathrm{MM}}(\mathbf{x}) = w_{\mathrm{I}}^{\mathrm{M}} + \sum_p \frac{\widehat{R}_p^{\mathrm{M}}}{\sqrt{|\widehat{\chi}_p|}} e^{\mathrm{i}\alpha_p x + \mathrm{i}\widehat{\chi}_p y}. \tag{5.3b}$$

On the bottom of the cell ($\mathbf{x} \in \gamma_-$), for a Helmholtz incident wave the total field is given by

$$w = \sum_p \frac{T_p^{\mathrm{H}}}{\sqrt{|\chi_p|}} e^{\mathrm{i}\alpha_p x - \mathrm{i}\chi_p y} + \sum_p \frac{\widehat{T}_p^{\mathrm{H}}}{\sqrt{|\widehat{\chi}_p|}} e^{\mathrm{i}\alpha_p x - \mathrm{i}\widehat{\chi}_p y} = w^{\mathrm{HH}}(\mathbf{x}) + w^{\mathrm{MH}}(\mathbf{x}), \tag{5.4}$$

and for a modified Helmholtz wave we have

$$w = \sum_p \frac{T_p^{\mathrm{M}}}{\sqrt{|\chi_p|}} e^{\mathrm{i}\alpha_p x - \mathrm{i}\chi_p y} + \sum_p \frac{\widehat{T}_p^{\mathrm{M}}}{\sqrt{|\widehat{\chi}_p|}} e^{\mathrm{i}\alpha_p x - \mathrm{i}\widehat{\chi}_p y} = w^{\mathrm{HM}}(\mathbf{x}) + w^{\mathrm{MM}}(\mathbf{x}), \tag{5.5}$$

where $T_p^{\mathrm{H}}, T_p^{\mathrm{M}}$ correspond to the Helmholtz component and $\widehat{T}_p^{\mathrm{H}}, \widehat{T}_p^{\mathrm{M}}$ correspond to the modified Helmholtz component of the field.

Applying Green's second identity to the central cell with our first test function (5.1a) and first pairing (H-H) reveals

$$\int_{\partial\Omega_0,\gamma_+,\gamma_-} \left\{ v_m^{\mathrm{H}} \partial_{n'} w^{\mathrm{HH}} - w^{\mathrm{HH}} \partial_{n'} v_m^{\mathrm{H}} \right\} dS' = 0. \tag{5.6a}$$

Note that these test functions ((5.1a) and (5.1b)) have the opposite quasi-periodicity to w^{HH}, w^{HM}, w^{MH} and w^{MM} and thus there is no contribution from γ_l and γ_r (the vertical sides of the cell).

It can be shown straightforwardly that the integral along γ_+ has the contribution

$$\int_{\gamma_+} \left\{ v_m^{\mathrm{H}}(\mathbf{x}') \partial_{n'} w^{\mathrm{HH}}(\mathbf{x}') - w^{\mathrm{HH}}(\mathbf{x}') \partial_{n'} v_m^{\mathrm{H}}(\mathbf{x}') \right\} dS' = d \left[\frac{-\mathrm{i}(\chi_0 + \mu_0)}{\sqrt{|\chi_0|}\sqrt{|\mu_0|}} e^{-\mathrm{i}(\chi_0 - \mu_0)y'} \delta_{m0} + \frac{\mathrm{i} R_m^{\mathrm{H}} (\chi_m - \mu_m)}{\sqrt{|\chi_m|}\sqrt{|\mu_m|}} e^{\mathrm{i}(\chi_m + \mu_m)y'} \right], \tag{5.6b}$$

where $y' = d/2$, and similarly that γ_- has the contribution

$$\int_{\gamma_-} \left\{ v_m^{\mathrm{H}}(\mathbf{x}') \partial_{n'} w^{\mathrm{HH}}(\mathbf{x}') - w^{\mathrm{HH}}(\mathbf{x}') \partial_{n'} v_m^{\mathrm{H}}(\mathbf{x}') \right\} dS' = d \left[\frac{\mathrm{i} T_m^{\mathrm{H}} (\chi_m + \mu_m)}{\sqrt{|\chi_m|}\sqrt{|\mu_m|}} e^{-\mathrm{i}(\chi_m - \mu_m)y''} \right], \tag{5.6c}$$

where $y'' = -d/2$. Therefore (5.6a) is of the form:

$$d \left[\frac{-\mathrm{i}(\chi_0 + \mu_0)}{\sqrt{|\chi_0|}\sqrt{|\mu_0|}} e^{-\mathrm{i}(\chi_0 - \mu_0)y'} \delta_{m0} + \frac{\mathrm{i} R_m^{\mathrm{H}} (\chi_m - \mu_m)}{\sqrt{|\chi_m|}\sqrt{|\mu_m|}} e^{\mathrm{i}(\chi_m + \mu_m)y'} + \frac{\mathrm{i} T_m^{\mathrm{H}} (\chi_m + \mu_m)}{\sqrt{|\chi_m|}\sqrt{|\mu_m|}} e^{-\mathrm{i}(\chi_m - \mu_m)y''} \right] - \int_{\partial\Omega_0} \left\{ v_m^{\mathrm{H}}(\mathbf{x}') \partial_{n'} w^{\mathrm{HH}}(\mathbf{x}') - w^{\mathrm{HH}}(\mathbf{x}') \partial_{n'} v_m^{\mathrm{H}}(\mathbf{x}') \right\} dS' = 0, \tag{5.6d}$$

where the final integral is oriented anticlockwise, and must be evaluated numerically as it depends on the geometry of the scatterer. Specifying $\mu_m = \chi_m$ for all m and $\mu_m = -\chi_m$ for all m reveals

$$T_m^{\mathrm{H}} = \delta_{m0} + \frac{|\chi_m|}{2\mathrm{i}d\chi_m} \int_{\partial\Omega_0} \left\{ v_m^{\mathrm{H}}(\mathbf{x}'; \chi_m) \partial_{n'} w^{\mathrm{HH}}(\mathbf{x}') - w^{\mathrm{HH}}(\mathbf{x}') \partial_{n'} v_m^{\mathrm{H}}(\mathbf{x}'; \chi_m) \right\} dS', \tag{5.7a}$$

$$R_m^{\mathrm{H}} = \frac{|\chi_m|}{2\mathrm{i}d\chi_m} \int_{\partial\Omega_0} \left\{ v_m^{\mathrm{H}}(\mathbf{x}'; -\chi_m) \partial_{n'} w^{\mathrm{HH}}(\mathbf{x}') - w^{\mathrm{HH}}(\mathbf{x}') \partial_{n'} v_m^{\mathrm{H}}(\mathbf{x}'; -\chi_m) \right\} dS', \tag{5.7b}$$

respectively. Similarly, for the M-M case we use the second test function (5.1b) and specify $\mu_m = \widehat{\chi}_m$ and $\mu_m = -\widehat{\chi}_m$ to obtain

$$\widehat{T}_m^{\mathrm{M}} = \delta_{m0} - \frac{1}{2d} \int_{\partial\Omega_0} \left\{ v_m^{\mathrm{M}}(\mathbf{x}'; \widehat{\chi}_m) \partial_{n'} w^{\mathrm{MM}}(\mathbf{x}') - w^{\mathrm{MM}}(\mathbf{x}') \partial_{n'} v_m^{\mathrm{M}}(\mathbf{x}'; \widehat{\chi}_m) \right\} dS', \tag{5.8a}$$

$$\widehat{R}_m^{\mathrm{M}} = -\frac{1}{2d} \int_{\partial\Omega_0} \left\{ v_m^{\mathrm{M}}(\mathbf{x}'; -\widehat{\chi}_m) \partial_{n'} w^{\mathrm{MM}}(\mathbf{x}') - w^{\mathrm{MM}}(\mathbf{x}') \partial_{n'} v_m^{\mathrm{M}}(\mathbf{x}'; -\widehat{\chi}_m) \right\} dS', \tag{5.8b}$$

respectively. Integrating around the fundamental cell for the H-M case with the first test function (5.1a) reveals

$$T_m^{\mathrm{M}} = \frac{|\chi_m|}{2\mathrm{i}d\chi_m}\int_{\partial\Omega_0}\left\{v_m^{\mathrm{H}}(\mathbf{x}';\,\chi_m)\partial_{n'}w^{\mathrm{HM}}(\mathbf{x}') - w^{\mathrm{HM}}(\mathbf{x}')\partial_{n'}v_m^{\mathrm{H}}(\mathbf{x}';\,\chi_m)\right\}dS', \tag{5.9a}$$

$$R_m^{\mathrm{M}} = \frac{|\chi_m|}{2\mathrm{i}d\chi_m}\int_{\partial\Omega_0}\left\{v_m^{\mathrm{H}}(\mathbf{x}';\,-\chi_m)\partial_{n'}w^{\mathrm{HM}}(\mathbf{x}') - w^{\mathrm{HM}}(\mathbf{x}')\partial_{n'}v_m^{\mathrm{H}}(\mathbf{x}';\,-\chi_m)\right\}dS'. \tag{5.9b}$$

Similarly, for the M-H case using the second test function (5.1b) we have

$$\widehat{T}_m^{\mathrm{H}} = -\frac{1}{2d}\int_{\partial\Omega_0}\left\{v_m^{\mathrm{M}}(\mathbf{x}';\,\widehat{\chi}_m)\partial_{n'}w^{\mathrm{MH}}(\mathbf{x}') - w^{\mathrm{MH}}(\mathbf{x}')\partial_{n'}v_m^{\mathrm{M}}(\mathbf{x}';\,\widehat{\chi}_m)\right\}dS', \tag{5.10a}$$

$$\widehat{R}_m^{\mathrm{H}} = -\frac{1}{2d}\int_{\partial\Omega_0}\left\{v_m^{\mathrm{M}}(\mathbf{x}';\,-\widehat{\chi}_m)\partial_{n'}w^{\mathrm{MH}}(\mathbf{x}') - w^{\mathrm{MH}}(\mathbf{x}')\partial_{n'}v_m^{\mathrm{M}}(\mathbf{x}';\,-\widehat{\chi}_m)\right\}dS'. \tag{5.10b}$$

Using the expressions above, one can construct $\mathbf{R}^{(0)}$ and $\mathbf{T}^{(0)}$ which denote the basic reflection and transmission matrices of a single grating for a wave travelling in the direction $y < 0$ (that is, from above). These matrices are given by

$$\mathbf{R}^{(0)} = \left[\begin{array}{c|c}\mathbf{R}_{\mathrm{HH}}^{(0)} & \mathbf{R}_{\mathrm{HM}}^{(0)}\\ \hline \mathbf{R}_{\mathrm{MH}}^{(0)} & \mathbf{R}_{\mathrm{MM}}^{(0)}\end{array}\right], \quad \text{and} \quad \mathbf{T}^{(0)} = \left[\begin{array}{c|c}\mathbf{T}_{\mathrm{HH}}^{(0)} & \mathbf{T}_{\mathrm{HM}}^{(0)}\\ \hline \mathbf{T}_{\mathrm{MH}}^{(0)} & \mathbf{T}_{\mathrm{MM}}^{(0)}\end{array}\right], \tag{5.11}$$

and have a phase origin at the centre of each scatterer (note the phase origin denotes the point from which phases are measured). Here the (p, q)th element of $\mathbf{R}_{\mathrm{HH}}^{(0)}$ is R_p^{H} which corresponds to the incident wave $w_{\mathrm{I}}^{\mathrm{H}}$ travelling down the channel, or grating order, $\alpha_q = \alpha_0 + 2\pi q/d$. Likewise, the (p, q)th element of $\mathbf{R}_{\mathrm{MH}}^{(0)}$ is $\widehat{R}_p^{\mathrm{H}}$ corresponding to $w_{\mathrm{I}}^{\mathrm{H}}$ down the channel α_q. Finally, the (p, q)th elements of $\mathbf{R}_{\mathrm{HM}}^{(0)}$ and $\mathbf{R}_{\mathrm{MM}}^{(0)}$ are R_p^{M} and $\widehat{R}_p^{\mathrm{M}}$ respectively, corresponding to $w_{\mathrm{I}}^{\mathrm{M}}$ down channel α_q. The transmission matrix $\mathbf{T}^{(0)}$ is created in an analogous manner to the definitions above.

Once formed, these matrices can then be shifted to the appropriate phase origins at $\mathbf{x} \in \gamma^+$ and $\mathbf{x} \in \gamma^-$ via the appropriate matrix multiplication:

$$\mathbf{T} = \mathbf{P}\mathbf{T}^{(0)}\mathbf{P}, \quad \text{and} \quad \mathbf{R} = \mathbf{P}\mathbf{R}^{(0)}\mathbf{P}, \tag{5.12a}$$

where

$$\mathbf{P} = \left[\begin{array}{c|c}\mathbf{P}^{\mathrm{H}} & \mathbf{0}\\ \hline \mathbf{0} & \mathbf{P}^{\mathrm{M}}\end{array}\right], \quad \mathbf{P}_{pq}^{\mathrm{H}} = \delta_{pq}e^{\mathrm{i}\chi_p d/2}, \quad \text{and} \quad \mathbf{P}_{pq}^{\mathrm{M}} = \delta_{pq}e^{\mathrm{i}\widehat{\chi}_p d/2}. \tag{5.12b}$$

6. Energy balance equations

As a check on numerics we use the previously computed conservation of energy relation as given in (7.3) of Movchan *et al.* (**8**) for a single grating. We express it in the following matrix form:

$$\mathbf{R}^{\mathrm{T}}\mathbf{U}\mathbf{R}^* + \mathbf{T}^{\mathrm{T}}\mathbf{U}\mathbf{T}^* = \mathbf{U} - \mathrm{i}\left(\mathbf{V}\mathbf{R}^* - \mathbf{R}^{\mathrm{T}}\mathbf{V}^{\mathrm{T}}\right), \tag{6.1}$$

where

$$\mathbf{U} = \left[\begin{array}{c|c} \mathbf{U}^{\mathrm{H}} & \mathbf{0} \\ \hline \mathbf{0} & \mathbf{0} \end{array}\right], \quad \mathbf{V} = \left[\begin{array}{c|c} \mathbf{V}^{\mathrm{H}} & \mathbf{0} \\ \hline \mathbf{0} & \mathbf{V}^{\mathrm{M}} \end{array}\right], \tag{6.2a}$$

$$\mathbf{U}^{\mathrm{H}}_{pq} = \beta_p \delta_{pq}, \quad \mathbf{V}^{\mathrm{H}}_{pq} = (\beta_p - 1)\delta_{pq}, \quad \mathbf{V}^{\mathrm{M}}_{pq} = \delta_{pq}, \quad \beta_n = \begin{cases} 1, & \alpha_n^2 \leq k^2 \\ 0, & \alpha_n^2 > k^2, \end{cases} \tag{6.2b}$$

and star notation represents a complex conjugate operation. The relation (6.2a) is satisfied independent of the order of truncation, as our method of interface matching in Section 5 ensures the fluxes are matched perfectly (**42**, **43**).

7. Platonic band surface calculation

The procedure for calculating band surfaces using scattering matrices is outlined in Botten *et al.* (**34**) for the case of a general photonic crystal array, and a brief outline is included here for the specific case of a square platonic lattice.

We begin by constructing horizontal lines above and below the central grating which sit halfway between the subsequent layers, and coincide with the top and bottom of the fundamental cell discussed earlier. These lines are introduced in order to shift the phase origin from the centre of each scatterer to $(x, y) = (x, \pm d/2)$. We introduce p_1 and p_2 to represent these two interfaces (above and below, respectively) and note that there are fields travelling across each line in the directions $y > 0$ and $y < 0$ (denoted by $\pm$, respectively). This admits the following representation of the displacement at each interface which is given by

$$w^j(\mathbf{x}) = \sum_{p=-\infty}^{\infty} \frac{1}{\sqrt{|\chi_p|}} \left(f_p^{(j)-} e^{-\mathrm{i}\chi_p(y-y_j)} + f_p^{(j)+} e^{\mathrm{i}\chi_p(y-y_j)} \right) e^{\mathrm{i}\alpha_p x} + \frac{1}{\sqrt{|\widehat{\chi}_p|}} \left(g_p^{(j)-} e^{-\mathrm{i}\widehat{\chi}_p(y-y_j)} + g_p^{(j)+} e^{\mathrm{i}\widehat{\chi}_p(y-y_j)} \right) e^{\mathrm{i}\alpha_p x}, \tag{7.1}$$

where $j = 1$ and $j = 2$ denote the lines p_1 and p_2, respectively, and $f_p^{(j)\pm}$, $g_p^{(j)\pm}$ denote the wave amplitudes of the Helmholtz and modified Helmholtz wave components, respectively.

Introducing the column vector $\mathbf{h}_j^{\pm} = [f_p^{(j)\pm}, g_p^{(j)\pm}]^{\mathrm{T}}$ for compactness, it is then possible to construct a scattering matrix which connects incoming with outgoing fields, that is

$$\left[\begin{array}{c} \mathbf{h}_2^- \\ \mathbf{h}_1^+ \end{array}\right] = \left[\begin{array}{c|c} \mathbf{T} & \mathbf{R}' \\ \hline \mathbf{R} & \mathbf{T}' \end{array}\right] \left[\begin{array}{c} \mathbf{h}_1^- \\ \mathbf{h}_2^+ \end{array}\right], \tag{7.2}$$

where $\mathbf{R}$ and $\mathbf{T}$ are the reflection and transmission matrices for an incident wave from above the grating, and $\mathbf{R}'$ and $\mathbf{T}'$ the appropriate matrices for an incident wave from below the grating. We observe that for y-symmetric scatterers in a square lattice, the matrices corresponding to an incident wave from below are the same as those from above, and so $\mathbf{R} = \mathbf{R}'$ and $\mathbf{T} = \mathbf{T}'$.

It is also possible to connect the fields travelling up and down the y-axis by imposing a quasi-periodicity condition in the y-direction:

$$\mathbf{h}_2^- = \mu \mathbf{h}_1^-, \qquad \text{and} \qquad \mathbf{h}_2^+ = \mu \mathbf{h}_1^+, \tag{7.3}$$

which arises from the fact that there is only a phase difference in the solution across the cell. Here $\mu = e^{-\mathrm{i}\kappa_y d}$ and κ_y is the unknown y-component of the Bloch vector $\boldsymbol{\kappa} = (\kappa_x, \kappa_y) = (\alpha_0, \kappa_y)$, and consequently (7.2) can be expressed as

$$\left[\begin{array}{c|c} \mathbf{T} - \mu\mathbf{I} & \mathbf{R} \\ \hline \mathbf{R} & \mathbf{T} - \mu^{-1}\mathbf{I} \end{array}\right] \begin{bmatrix} \mathbf{h}_1^- \\ \mathbf{h}_2^+ \end{bmatrix} = \mathbf{0}. \tag{7.4}$$

We then define $P(\mu)$ as the determinant of the above block-matrix system and seek values of μ such that $P(\mu) = 0$. Note that due to the lattice symmetry we have pairings of zeros $P(\mu) = P(1/\mu)$.

Botten *et al.* (**34**) then propose an efficient representation of such symmetric geometries by applying a unitary transformation to (7.4), which halves the dimension of the block-matrix system (7.4) by converting the system into a pair of equivalent eigenvalue equations. Either of these systems can then be solved to yield the unknown μ, and we specify the first system here for compactness:

$$\mathbf{S}^{-1}\mathbf{T}\mathbf{g} = \frac{1}{2c}\mathbf{g}, \tag{7.5}$$

where for our purposes $\mathbf{g}$ denotes an arbitrary eigenvector, $2c = \mu + \mu^{-1}$, and

$$\mathbf{S} = \mathbf{I} + (\mathbf{T} - \mathbf{R})(\mathbf{T} + \mathbf{R}). \tag{7.6}$$

Providing $c \in \mathbb{R}$, then eigenvalues with $|c| \leq 1$ correspond to real or propagating states, and hence, admissable phase factors μ. If $c \in \mathbb{C}$ or $|c| > 1$ then we have a phase factor which corresponds to an evanescent or non-propagating state. In other words, once the eigenvalues $\lambda = 1/2c$ have been found, we merely need to solve the simple quadratic equation $\mu^2 - 2c\mu + 1 = 0$ to reveal values of μ which are associated with propagating Bloch modes.

Solving our eigenvalue problem above reveals eigenvalues $\mu = e^{-\mathrm{i}\kappa_y d}$, and so we can easily see that

$$\kappa_y = \mathrm{Re}\left[\frac{\mathrm{i}}{d}\log(\mu)\right], \quad \text{or equivalently,} \quad \kappa_y = -\arg(\mu)/d, \tag{7.7}$$

which are our unknown Bloch vector elements.

For a scatterer of arbitrary shape (that is no y-symmetry) the system to be solved is

$$\left[\begin{array}{c|c} \mathbf{T} - \mathbf{R}'\mathbf{T}'^{-1}\mathbf{R} & \mathbf{R}'\mathbf{T}'^{-1} \\ \hline -\mathbf{T}'^{-1}\mathbf{R} & \mathbf{T}'^{-1} \end{array}\right] \begin{bmatrix} \mathbf{h}_1^- \\ \mathbf{h}_2^+ \end{bmatrix} = \mu \begin{bmatrix} \mathbf{h}_1^- \\ \mathbf{h}_2^+ \end{bmatrix}, \tag{7.8}$$

which directly reveals the unknown Bloch factors as eigenvalues. That said, computing the matrix $\mathbf{T}'^{-1}$ requires some care, as it is less numerically stable than (7.5).

8. Results and discussion

We begin by computing the first band surfaces for a range of scattering geometries which exhibit four-fold three-fold and two-fold symmetry, as seen in Fig. 2. We assume a grating period of $d = 1$, discretise the scatterer boundaries with 700 panels at the edge and consider 2 propagating orders (that is, $m = -2$ to 2) when constructing the reflection and transmission matrices. We find that this number of panels and orders is sufficient to ensure good convergence of the reflection and transmission coefficients (5.7a)–(5.10b) across all geometries.

All of the scatterers in Fig. 2 have been created to approximately preserve the area associated with a circle of radius $a = 0.2$. The scale of these geometries is determined using the Shoelace algorithm (**44**) for a large number of points at the boundary edge and so we introduce the parametric form:

$$(x, y) = (a\, r(\theta)\cos(\theta), b\, r(\theta)\sin(\theta)), \tag{8.1}$$

to construct our scatterers. For the circular scatterer in Fig. 2(a) we simply specify $a = b = 0.2$ and $r(\theta) = 1$, for the L4 geometry shown in Fig. 2(b) we have

$$r(\theta) = \left(\frac{1}{\cos^4(\theta) + \sin^4(\theta)}\right)^{1/4}, \quad \text{and} \quad a = b = 0.1841, \tag{8.2a}$$

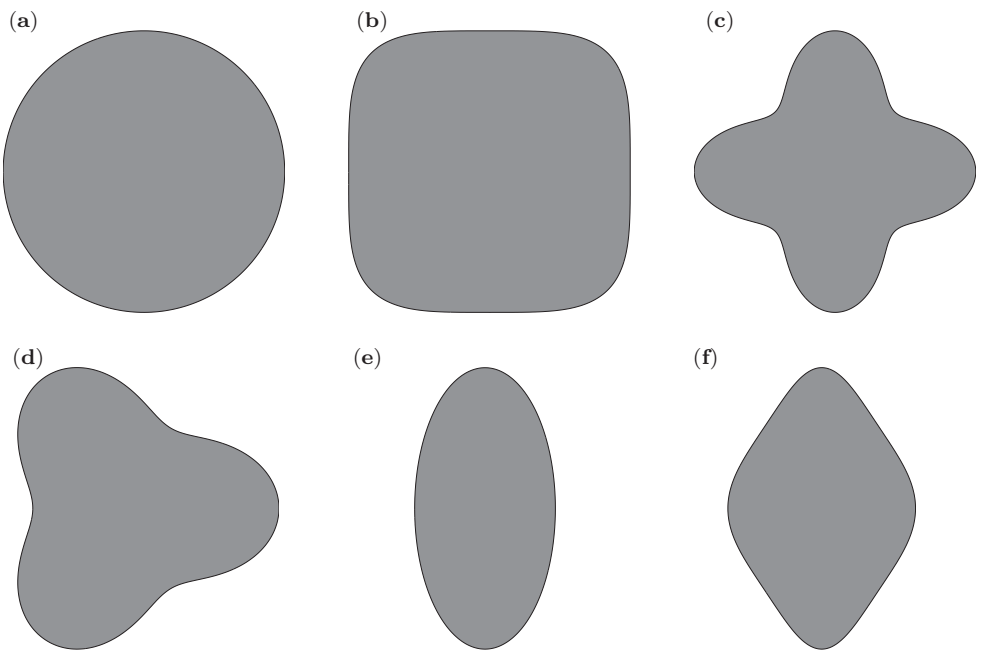

Fig. 2 Scattering geometries considered: (a) circle; (b) L4 or rounded square; (c) four-leaf clover; (d) three leaf clover; (e) ellipse ($b/a = 2$); and (f) diamond

for the four-leaf clover in Fig. 2(c) we have

$$r(\theta) = 4 + \cos(4\theta), \quad \text{and} \quad a = b = 0.0493, \tag{8.2b}$$

for the three-leaf clover in Fig. 2(d) we have

$$r(\theta) = 4 + \cos(3\theta), \quad \text{and} \quad a = b = 0.0493, \tag{8.2c}$$

and for the ellipse ($b/a = 2$) in Fig. 2(e) we have $a = 0.1414$, $b = 0.2828$ and $r(\theta) = 1$. The final diamond geometry is formed via

$$(x, y) = \left(\frac{a}{\sqrt{2}} r(\theta) \{\cos(\theta) - \sin(\theta)\}, \frac{3a}{2\sqrt{2}} r(\theta) \{\cos(\theta) + \sin(\theta)\} \right), \tag{8.2d}$$

where $a = 0.1504$ and the $r(\theta)$ expression from (8.2a) is used. Here the rounded square scatterer is referred to as an L4 geometry due to its association with the L4 norm ($x^4 + y^4 = 1$).

In Fig. 3 we construct the first band surfaces for these geometries. In Figs 3(a) to (c) we see band surfaces which exhibit qualitatively similar curvatures, which one would expect for geometries that exhibit four-fold symmetry and have aspect ratio close to 1 (that is, compact geometry). They each feature a maximum at the origin, a total of four minima at $(\kappa_x, \kappa_y) = (\pm\pi, \pm\pi)$ and four saddle points at $(\kappa_x, \kappa_y) = (0, \pm\pi)$ and $(\kappa_x, \kappa_y) = (\pm\pi, 0)$. For the circular scatterer we have a relative maximum value of $k = 5.6554$ and relative minima values of $k = 5.5677$, for the L4 geometry we have a maximum value of $k = 5.7482$ and minima values of $k = 5.7051$ and for the four-leaf clover a maximum value of $k = 5.7703$ with minima values of $k = 5.5549$. The isofrequency contours of these band surfaces are largely circular in nature, and as such the array is said to act as an isotropic medium (that is, the group velocity vector is parallel to the the crystal wave vector (**45**)). The frequency ranges for these three geometries does vary, and the band surface with the smallest k-range is the L4 geometry which corresponds to low magnitude group velocity vectors and thus, slower wave energy propagation through the array. The contours for the four-leaf clover scatterer in Fig. 3(c) do exhibit sharper contours near the saddle points, but still remain qualitatively similar to the other shapes exhibiting four-fold symmetry. In Fig. 3(c) we have the band surface for a three-leaf clover shape, which is related to the previous figures and possesses the same number of critical points (with a maximum of $k = 5.8332$ and minima at $k = 5.7224$). However, it does not exhibit perfect isotropy as the contours (especially near the origin) are slightly elliptical. Additionally the band surface does not exhibit up-down or left-right symmetry as a result of the scattering geometry and so the contours for $\kappa_y > 0$ can be obtained by rotation and reflection of the band surface picture obtained for $\kappa_y < 0$. These first four scatterers all possess regions where negative refraction through their respective arrays is supported, which are characterised by diagonally sloping contours, as seen in (**15**).

In Fig. 3(e) we see the band surface for an ellipse ($b/a = 2$) which exhibits very different behaviour compared to the previous geometries. This band surface now features two maxima at $(\kappa_x, \kappa_y) = (0, \pm\pi)$, two minima at $(\kappa_x, \kappa_y) = (\pm\pi, 0)$ and saddle points at both the origin and at the extreme corners of the Brillouin zone. The array exhibits extremely anisotropic behaviour, however isotropic contours are seen in the vicinity of the minima. It also exhibits preferential directions of propagation—that is, at low k-values the array (below $k = 5.6175$) favours horizontal propagation through the platonic crystal, and at high k-values (above $k = 5.6175$), it favours vertical propagation through the

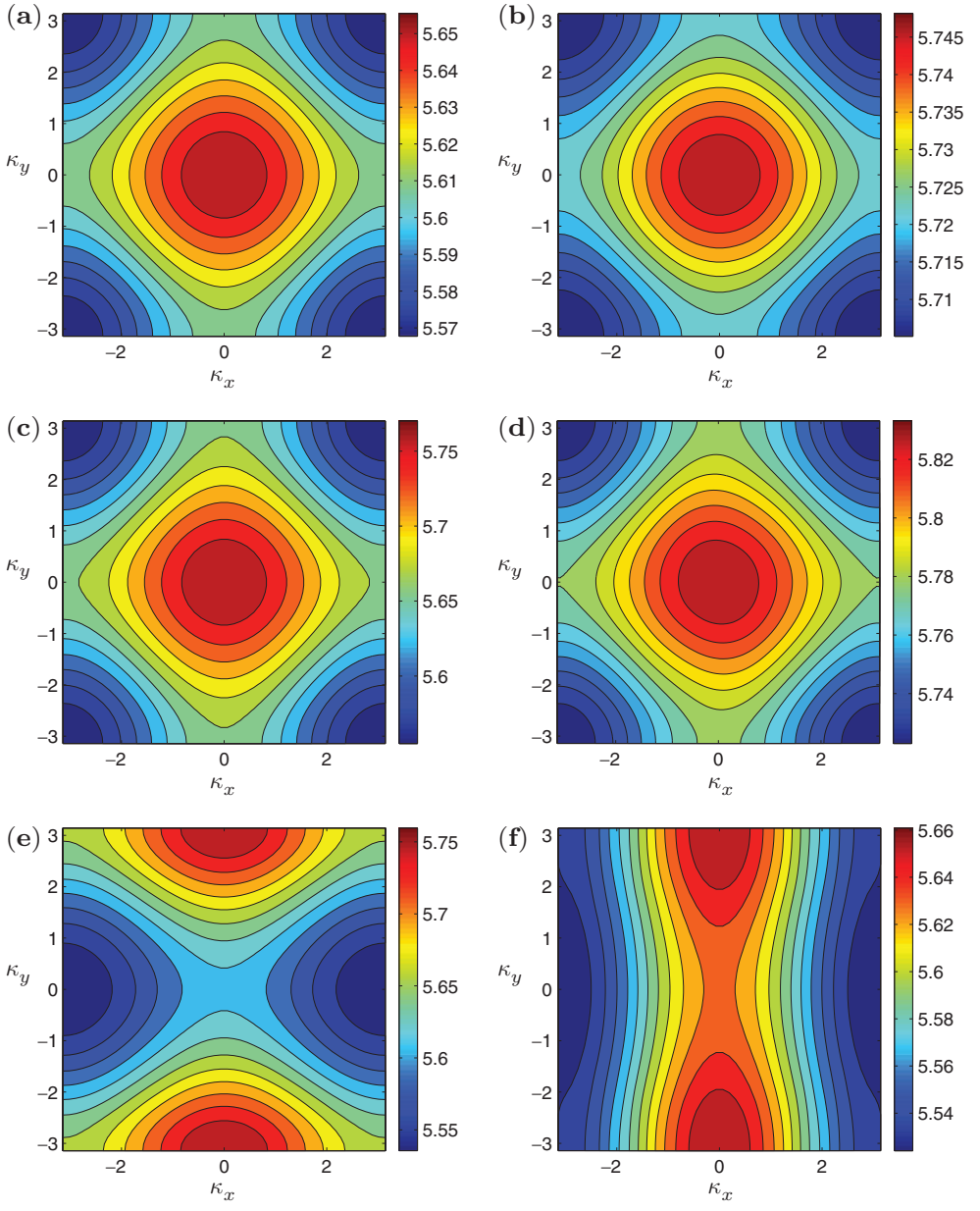

Fig. 3 Isofrequency contours of the first band surface for the geometry: (a) circle ($a = 0.2$); (b) L4 shape; (c) four-leaf clover; (d) three-leaf clover; (e) ellipse; and (f) diamond

crystal. We refer to structures which exhibit strong preferential directions of propagation as platonic polarisers, in an analogous manner to their optical counterparts. A similar picture is seen for the case of a diamond geometry in Fig. 3(f), except that the contours strongly favour horizontal propagation through the array as opposed to vertical (which is only seen in a small window around $\kappa_x = 0$ for $k > 5.6135$). As with the elliptical scatterer we have two maxima ($k = 5.6609$) and two minima ($k = 5.5241$), as well as saddle points at the origin and extreme corners of the Brillouin zone. If we were to rotate the diamond by 90° to a horizontal position, the associated band surface would also rotate by the same angle. In such an instance, we would see wide intervals where ultrarefraction is supported due to the very flat contours seen here (note that ultrarefraction is defined in the photonics literature as angles of refraction $\theta_c \simeq 0$ (**46**)).

We also construct the band surfaces for these same geometries in Fig. 4, but they are now scaled to the area of circle of radius $a = 0.1$. Here the band surfaces for scatterers with four- and three-fold symmetry now bear similarity to the first band surface associated with square arrays of pins, as seen in Smith *et al.* (**15**). That is, in Fig. 4(a) we have absolute maxima at $(\kappa_x, \kappa_y) = (\pm\pi, \pm\pi)$ of $k = 4.7211$, absolute minima at $(\kappa_x, \kappa_y) = (0, \pm\pi)$ and $(\kappa_x, \kappa_y) = (0, \pm\pi)$ of $k = 4.5511$ and a relative maxima at the origin of $k = 4.5643$. Similarly in Fig. 4(b) the band surface has an absolute maximum of $k = 4.7538$, minimum of $k = 4.5670$ and relative maximum of $k = 4.5868$ at these same coordinates and in Fig. 4(c) we have an absolute maximum of $k = 4.7224$, minimum of $k = 4.6295$ and relative maximum of $k = 4.6597$ at these points. For Fig. 4(d) associated with the three-leaf clover geometry we have a clear break in up-down symmetry, but still retain relative maxima at the extreme edge of the Brillouin zone of $k = 4.7572$, relative minima at $(0, \pm\pi)$ and $(\pm\pi, 0)$ of $k = 4.6194$ and a relative maximum at the origin of $k = 4.6379$.

For the ellipse in Fig. 4(e) and the diamond in Fig. 4(f) there is still a pronounced difference in band surface curvature compared with the more compact geometries, except that we now have relative maxima in the extreme edges of the Brillouin zone. For the case of the ellipse, we still see horizontal propagation as the preferred direction for values below the central saddle point (that is, $k = 4.6150$) and vertical propagation as the preferred direction for values above $k = 4.6150$ with $\theta_c \simeq 0$, that is ultrarefractive properties. In total, we have four relative maxima at $(\pm\pi, \pm\pi)$ with $k = 4.7538$ and two minima at $(0, \pm\pi)$ for $k = 4.4800$. There are also two saddle points at $(\pm\pi, 0)$. A similar picture is seen for the diamond scatterer with absolute maximum values of $k = 4.7191$, minimum values of $k = 4.4946$ and a central saddle point value of $k = 4.6015$.

Consequently, it would seem that band surfaces for scatterers with large aspect ratios (that is, long and slender scatterers) have very different isofrequency contours compared to those of more compact geometry, acting as platonic polarisers and ultrarefractive media. Another interesting feature for all of the clamped geometries considered is the presence of a stop band below the first band surface (at low k) which persists even as we shrink the area of the scatterer down to zero (that is, consider a pinned inclusion) (**9**).

In Fig. 5 we examine vertical slices of the band surfaces as we transition from circular to elliptical scatterers (while preserving area) at $\kappa_x = 0$ and $\kappa_x = \pi$. Here we see the platonic polariser effect becoming more pronounced as b/a is increased. We also see what appears to be an ultraflat band near $b/a = 1.2$. However, in Fig. 5(a) we have a minimum range of k at $b/a = 1.2218$ and in Fig. 5(b) we have a minimum range of k at $b/a = 1.2414$ which suggests that there is always a degree of curvature present in the band surfaces associated with an ellipse. If we examine the average curvature across these segments, we see a minimum value of 0.0026 at $b/a = 1.2$ for $\kappa_x = 0$ and a minimum value of 0.0020 at $b/a = 1.2323$ for $\kappa_x = \pi$. We consequently propose that there exist ultraflat bands between these particular aspect ratios.

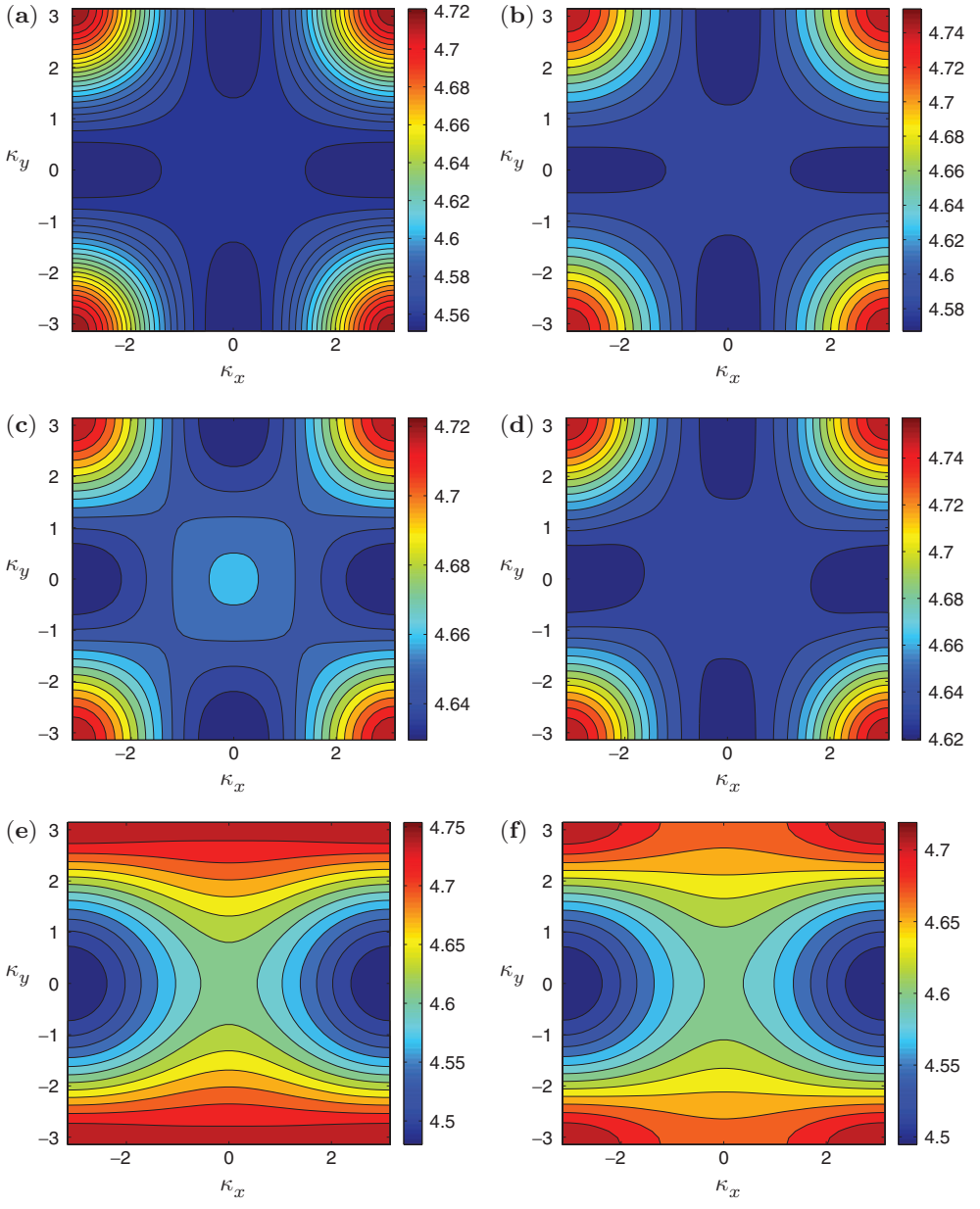

Fig. 4 Isofrequency contours of the first band surface for the geometry: (a) circle ($a = 0.1$); (b) L4 shape; (c) four-leaf clover; (d) three-leaf clover; (e) ellipse; and (f) diamond

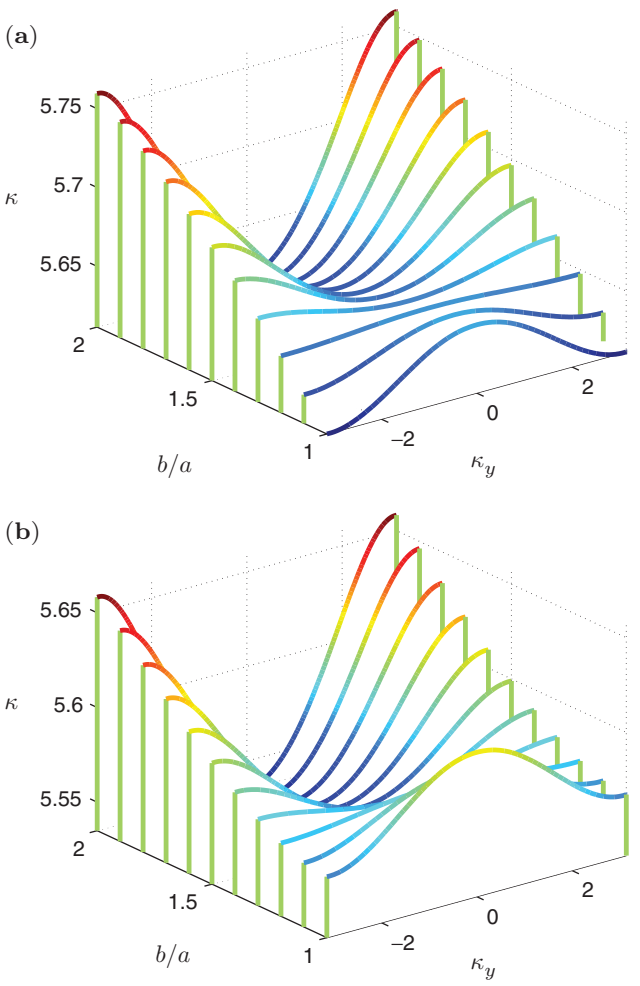

Fig. 5 Segments of the first band surface corresponding to (a) $\kappa_x = 0$ and (b) $\kappa_x = \pi$ for elliptical scatterers of constant area

In Fig. 6 we construct the band surfaces for an ellipse ($b/a = 2$, $a = 0.2$) when rotated by 30° in Fig. 6(a) and by 45° in Fig. 6(b), clockwise about the origin. Under rotation by 30° we see an increase in horizontal propagation preference as opposed the vertical direction, as well as a decrease in the k-range of the band. The maximum value of $k = 5.7630$ is achieved at $(0, \pm\pi)$ and the minimum values are at $(\pm\pi, 0)$ for $k = 5.6472$ with a central saddle value of $k = 5.7321$. For 45° rotation we see an increased degree of isotropy in the centre of the band surface compared to Fig. 3(e), however, the isofrequency contours are predominantly elliptic throughout. We have a central maximum of $k = 5.7815$, four minima of $k = 5.6748$ at the edges of the Brillouin zone and four saddle points.

In Table 1, we present a table of k-values corresponding to selected points throughout the Brillouin zone. The values obtained for the circular scatterer show good agreement with the values obtained

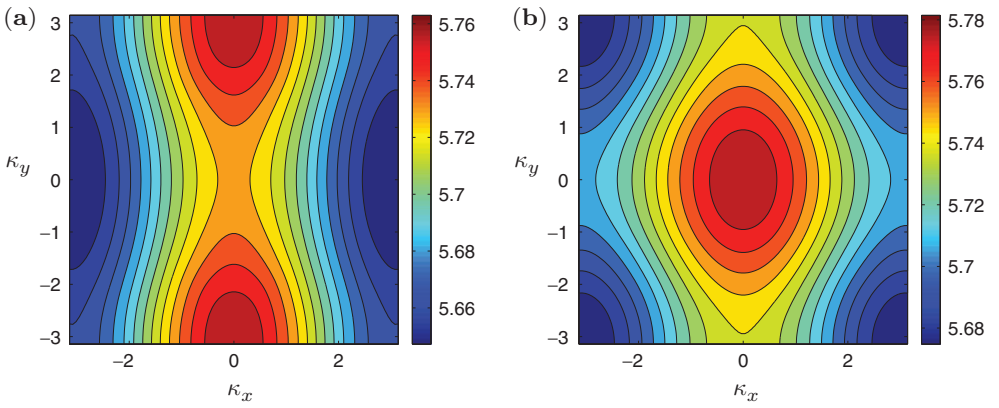

Fig. 6 Band surfaces corresponding to elliptical scatterers ($b/a = 2$, and scaled to a circle radius $a = 0.2$) rotated clockwise by (a) 30° and by (b) 45°

Table 1 Values of k for the first band surface corresponding to a square array of clamped scatterers. Here Coordinates 1, 2 and 3 refer to $(\kappa_x, \kappa_y) = (\pi/2, 0)$, $(\kappa_x, \kappa_y) = (\pi, \pi/2)$ and $(\kappa_x, \kappa_y) = (\pi/2, \pi/2)$, respectively

Scatterer		Coordinate		
		1	2	3
Circle ($a = 0.2$)	Present	5.634548	5.590603	5.613445
	Poulton *et al.* (**10**)	5.634877	5.590820	5.613727
L4 geometry		5.736497	5.714475	5.725981
Four-leaf clover		5.719556	5.612017	5.666343
Three-leaf clover		5.806273	5.751169	5.779585
Ellipse ($b/a = 2$)		5.576275	5.585914	5.630089
Diamond geometry		5.577697	5.530857	5.587417

in Poulton *et al.* (**10**), and are obtained by interpolation over the scattered data obtained using the procedure outlined in Section 7. These values are included for reference. A similar table of values is presented in Table 2 when the scatterers are scaled to preserve the area associated with a circle of radius $a = 0.1$.

In Fig. 7 we examine the reflection and transmission curves for a single grating of scatterers. In particular we consider $|R_0|$ and $|T_0|$ for a single array constructed of circles in Fig. 7(a), an array of three-leaf clovers in Fig. 7(b) and an array of ellipses ($b/a = 2$) in Fig. 7(c). We consider these coefficients over the range $\pi/2 < k < 3\pi$ as for $k \leq \pi/2$ we have $|T_0| \simeq 0$ and $|R_0| \simeq 1$ for all three geometries. In all three of these figures we can clearly see the effect of Wood anomalies on the

Table 2 Values of k for the first band surface corresponding to a square array of clamped scatterers scaled to preserve area of circle radius $a = 0.1$

Scatterer		Coordinate		
		1	2	3
Circle ($a = 0.1$)	Present	4.557725	4.615795	4.580976
	Poulton *et al.* (10)	4.557812	4.615857	4.581035
L4 geometry		4.580074	4.643568	4.605637
Four-leaf clover		4.645573	4.665761	4.653435
Three-leaf clover		4.629980	4.672998	4.649261
Ellipse ($b/a = 2$)		4.552513	4.578742	4.624228
Diamond geometry		4.552810	4.577746	4.606281

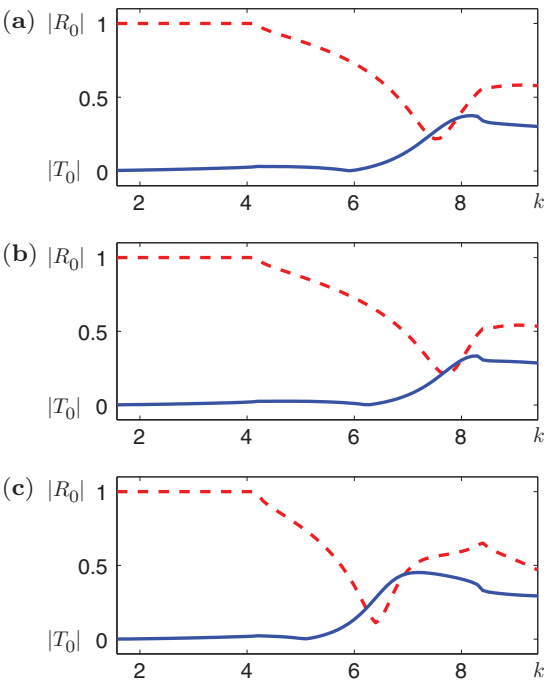

Fig. 7 Reflection and Transmission curves for a single grating constructed of (a) circles of radius $a = 0.2$; (b) three-leaf clovers; and (c) ellipses ($b/a = 2$) for a Helmholtz incident wave at $\theta_i = \pi/6$

reflection and transmission curves, as they become discontinuous at these points, creating pronounced dips and spikes in the curves. These Wood anomalies take place at $k = 4.1888$ and $k = 8.3776$ over this interval for the fixed incident angle $\theta_i = \pi/6$ (irrespective of geometry). For a circular grating we have a minimum in reflection of $|R_0| = 0.2156$ at $k = 7.5335$ and a minimum of transmission

($|T_0| \simeq 0$) at $k = 5.9228$. We have an interval of minimal transmission over $5.5677 < k < 5.6554$ which is associated with the first band surface for the doubly periodic array problem, and this is reflected in the array problem by group velocity vectors of small magnitude. For the three-leaf clover array in Fig. 7(b) we have a minimum value of reflection $|R_0| = 0.2059$ at $k = 7.7174$ and a minimum in transmission at $k = 6.2515$. For the elliptical grating we see stronger transmission compared to the other two curves which is characterised by a zero in transmission at $k = 5.0802$ and a maximum in transmission of $|T_0| = 0.4518$ at $k = 7.1934$, along with an earlier minimum value in reflection of $|R_0| = 0.1097$ at $k = 6.4118$.

9. Conclusions

In this article we have demonstrated how to construct the solution for both a grating and doubly periodic square array comprised of scatterers which are of arbitrary geometry. The solution is constructed using boundary integral equations, quasi-periodic Green's functions and scattering matrices, which have allowed us to find band surfaces for geometries of arbitrary shape. We have calculated the first band surfaces for a select number of geometries which have been shown to exhibit a number of complex scattering behaviours including negative refraction, preferential directions of propagation (acting as platonic polarisers), stop bands at low wave number, ultrarefraction and anisotropic wave propagation. There have also been a number of interesting behaviours associated with elliptical geometries, including induced isotropy under rotation and the existence of ultraflat bands. Future work includes the construction of band surfaces with free-edge boundary conditions at the edge, and an extension of the boundary integral theory outlined here to arrays of cracks of arbitrary path, in a related vein to work by Porter and Evans (**47**, **48**).

Acknowledgements

M.J.A.S. would like to acknowledge John D'Errico for the program *interparc.m* which ensures approximately equidistant discretisation of our scattering geometries (available at: *www.mathworks.com*).

References

1. C. Palmer, The baseline: diffraction gratings – the crucial dispersive component, *Spectroscopy* **10** (1995) 14–15.
2. E. Renzi and F. Dias, Relations for a periodic array of flap-type wave energy converters, *arXiv preprint* arXiv:1209.6303 (2012).
3. R. Martínez-Sala, C. Rubio, L. M. García-Raffi, J. V. Sánchez-Pérez, E. A. Sánchez-Pérez and J. Llinares, Control of noise by trees arranged like sonic crystals, *J. Sound. Vib.* **291** (2006) 100–106.
4. L. G. Bennetts and V. A. Squire, Wave scattering by multiple rows of circular ice floes, *J. Fluid Mech.* **639** (2009) 213–238.
5. J. D. Joannopoulos, *Photonic Crystals: Molding the Flow of Light* (Princeton University Press, Princeton 2008).
6. X. Hu, Y. Shen, X. Liu, R. Fu and J. Zi, Superlensing effect in liquid surface waves, *Phys. Rev. E* **69** (2004) 030201.

7. X. Zhang and Z. Liu, Negative refraction of acoustic waves in two-dimensional phononic crystals, *Appl. Phys. Lett.* **85** (2004) 341–343.
8. N. V. Movchan, R. C. McPhedran, A. B. Movchan and C. G. Poulton, Wave scattering by platonic grating stacks, *Proc. R. Soc. A* **465** (2009) 3383–3400.
9. A. B. Movchan, N. V. Movchan and R. C. McPhedran, Bloch–Floquet bending waves in perforated thin plates, *Proc. R. Soc. A* **463** (2007) 2505–2518.
10. C. G. Poulton, R. C. McPhedran, N. V. Movchan and A. B. Movchan, Convergence properties and flat bands in platonic crystal band structures using the multipole formulation, *Wave Random Complex* **20** (2010) 702–716.
11. M. Farhat, S. Guenneau and S. Enoch, High directivity and confinement of flexural waves through ultra-refraction in thin perforated plates, *Europhys. Lett.* **91** (2010) 54003.
12. T. Antonakakis and R. V. Craster, High–frequency asymptotics for microstructured thin elastic plates and platonics, *Proc. R. Soc. A* **468** (2012) 1408–1427.
13. R. C. McPhedran, A. B. Movchan and N. V. Movchan, Platonic crystals: Bloch bands, neutrality and defects, *Mech. Mater.* **41** (2009) 356–363.
14. D. V. Evans and R. Porter, Penetration of flexural waves through a periodically constrained thin elastic plate in vacuo and floating on water, *J. Eng. Math.* **58** (2007) 317–337.
15. M. J. A. Smith, R. C. McPhedran, C. G. Poulton and M. H. Meylan, Negative refraction and dispersion phenomena in platonic clusters, *Wave Random Complex* **22** (2012) 435–458.
16. S. G. Haslinger, N. V. Movchan, A. B. Movchan and R. C. McPhedran, Transmission, trapping and filtering of waves in periodically constrained elastic plates, *Proc. R. Soc. A* **468** (2012) 76–93.
17. M. J. A. Smith, M. H. Meylan and R. C. McPhedran, Scattering by cavities of arbitrary shape in an infinite plate and associated vibration problems, *J. Sound Vib.* **330** (2011) 4029–4046.
18. M. H. Meylan and R. C. McPhedran, Fast and slow interaction of elastic waves with platonic clusters, *Proc. R. Soc. A* **467** (2011) 3509–3529.
19. B. R. Mace, Periodically stiffened fluid-loaded plates, I: Response to convected harmonic pressure and free wave propagation, *J. Sound Vib.* **73** (1980) 473–486.
20. B. R. Mace, Periodically stiffened fluid-loaded plates. II: Response to line and point forces, *J. Sound. Vib.* **73** (1980) 487–504.
21. D. J. Mead and S. Parthan, Free wave propagation in two-dimensional periodic plates, *J. Sound. Vib.* **64** (1979) 325–348.
22. D. J. Mead, Plates with regular stiffening in acoustic media: vibration and radiation, *J. Acoust. Soc. Am.* **88** (1990) 391–401.
23. D. Gueorguiev, J. Gregory-McDaniel, P. DuPont and L. B. Felsen, Analysis of Floquet wave generation and propagation in a plate with multiple arrays of line attachments, *J. Sound. Vib.* **234** (2000) 819–840.
24. M. Spasenović, T. P. White, S. Ha, A. A. Sukhorukov, T. Kampfrath, Y. S. Kivshar, C. M. de Sterke, T. F. Krauss and L. Kuipers, Experimental observation of evanescent modes at the interface to slow-light photonic crystal waveguides, *Opt. Lett.* **36** (2011) 1170–1172.
25. A. Barnett and L. Greengard, A new integral representation for quasi-periodic scattering problems in two dimensions, *BIT* **51** (2011) 67–90.
26. A. Barnett and L. Greengard, A new integral representation for quasi-periodic fields and its application to two-dimensional band structure calculations, *J. Comput. Phys.* **229** (2010) 6898–6914.

27. K. Dossou, M. A. Byrne and L. C. Botten, Finite element computation of grating scattering matrices and application to photonic crystal band calculations, *J. Comput. Phys.* **219** (2006) 120–143.
28. C. M. Linton, The Green's function for the two-dimensional Helmholtz equation in periodic domains, *J. Eng. Math.* **33** (1998) 377–401.
29. R. C. McPhedran, N. A. Nicorovici, L. C. Botten and K. A. Grubits, Lattice sums for gratings and arrays, *J. Math. Phys.* **41** (2000) 7808–7816.
30. R. W. Wood, On a remarkable case of uneven distribution of light in a diffraction grating spectrum, *Philos. Mag. J. Sci.* **4** (1902) 396–402.
31. L. Rayleigh, Note on the remarkable case of diffraction spectra described by Prof. Wood, *Philos. Mag. J. Sci.* **14** (1907) 60–65.
32. M. Born and E. Wolf, *Principles of Optics: Electromagnetic Theory of Propagation and Diffraction of Light* (Pergamon Press, New York 1964).
33. O. P. Bruno and B. Delourme, Rapidly convergent quasi-periodic Green function throughout the spectrum – including Wood anomalies, *Unpublished online preprint*. Available online at: http://uma.ensta-paristech.fr/files/publis/2200/ (2012).
34. L. C. Botten, N. A. Nicorovici, R. C. McPhedran, C. M. de Sterke and A. A. Asatryan, Photonic band structure calculations using scattering matrices, *Phys. Rev. E* **64** (2001) 046603.
35. M. J. A. Smith, R. Porter and T. W. Williams, The effect on bending waves by defects in pinned elastic plates, *J. Sound. Vib.* **331** (2012) 5087–5106.
36. N. Gutman, C. M. de Sterke, A. A. Sukhorukov and L. C. Botten, Slow and frozen light in optical waveguides with multiple gratings: degenerate band edges and stationary inflection points, *Phys. Rev. A* **85** (2012) 033804.
37. N. Gutman, A. A. Sukhorukov, F. Eilenberger and C. M. de Sterke, Bistability suppression and low threshold switching using frozen light at a degenerate band edge waveguide, *Opt. Express* **20** (2012) 27363–27368.
38. L. C. Wrobel and M. H. Aliabadi, *The Boundary Element Method: Applications in Thermo-Fluids and Acoustics* (John Wiley & sons, Chichester 2002).
39. N. A. Nicorovici and R. C. McPhedran, Lattice sums for off-axis electromagnetic scattering by gratings, *Phys. Rev. E* **50** (1994) 3143–3160.
40. M. Abramowitz and I. A. Stegun, *Handbook of Mathematical Functions with Formulas, Graphs, and Mathematical Tables* (Dover publications, New York 1972).
41. V. Twersky, Elementary function representations of Schlömilch series, *Arch. Rational Mech. An.* **8** (1961) 323–332.
42. L. C. Botten, M. S. Craig, R. C. McPhedran, J. L. Adams and J. R. Andrewartha, The finitely conducting lamellar diffraction grating, *J. Mod. Optic.* **28** (1981) 1087–1102.
43. L. C. Botten and R. C. McPhedran, Completeness and modal expansion methods in diffraction theory, *J. Mod. Optic.* **32** (1985) 1479–1488.
44. D. Zwillinger, *CRC Standard Mathematical Tables and Formulae* (CRC Press, Boca Raton, FL 2011).
45. M. J. Steel, R. Zoli, C. Grillet, R. C. McPhedran, C. M. de Sterke, A. Norton, P. Bassi and B. J. Eggleton, Analytic properties of photonic crystal superprism parameters, *Phys. Rev. E* **71** (2005) 056608.
46. D. Maystre and S. Enoch, Perfect lenses made with left-handed materials: Alice's mirror? *J. Opt. Soc. Am. A* **21** (2004) 122–131.

47. R. Porter and D. V. Evans, Scattering of flexural waves by multiple narrow cracks in ice sheets floating on water, *Wave Motion* **43** (2006) 425–443.
48. R. Porter and D. V. Evans, Diffraction of flexural waves by finite straight cracks in an elastic sheet over water, *J. Fluid. Struct.* **23** (2007) 309–327.
49. S. K. Chin, N. A. Nicorovici and R. C. McPhedran, Green's function and lattice sums for electromagnetic scattering by a square array of cylinders, *Phys. Rev. E* **49** (1994) 4590–4602.

APPENDIX

Band surface calculation for circular cavities

For the particular case of an array of circular cavities one can represent the solution to (2.1) in terms of multipoles. This solution approach is outlined in Movchan *et al.* (**9**), Poulton *et al.* (**10**) and is included here as a check on numerics. Inside the fundamental Wigner–Seitz cell we can expand the homogeneous solution as

$$w(\mathbf{x}) = \sum_{n=-\infty}^{\infty} \left(A_n J_n(kr) + B_n I_n(kr) + E_n H_n^{(1)}(kr) + F_n K_n(kr) \right) e^{\mathrm{i}n\theta}. \tag{A.1}$$

After imposing the clamped-edge conditions (3.1) at $r = a$, we obtain the system

$$A_n J_n(ka) + B_n I_n(ka) + E_n H_n^{(1)}(ka) + F_n K_n(ka) = 0, \tag{A.2}$$

$$A_n J_n'(ka) + B_n I_n'(ka) + E_n H_n^{(1)\prime}(ka) + F_n K_n'(ka) = 0, \tag{A.3}$$

where prime notation denotes derivatives with respect to r. This can then be solved after substitution of the appropriate dynamic Rayleigh identities:

$$A_n = \sum_{l=-\infty}^{\infty} (-1)^{l-n} S_{l-n}^{\mathrm{H,A}} E_l, \quad \text{and} \quad B_n = \sum_{l=-\infty}^{\infty} (-1)^{l} S_{l-n}^{\mathrm{K,A}} F_l. \tag{A.4}$$

Here $S_l^{\mathrm{H,A}}$ and $S_l^{\mathrm{K,A}}$ are lattice (array) sums as opposed to grating sums, which are given in convergent form by

$$S_m^{\mathrm{H,A}}(k, \boldsymbol{\kappa}) = -\delta_{m0} + \mathrm{i} S_m^{\mathrm{Y,A}}(k, \boldsymbol{\kappa}), \tag{A.5}$$

$$S_m^{\mathrm{Y,A}}(k, \boldsymbol{\kappa}) = \frac{1}{J_{m+3}(k\xi)} \left(- \left[Y_3(k\xi) + \frac{1}{\pi} \sum_{n=1}^{3} \frac{(3-n)!}{(n-1)!} \left(\frac{2}{k\xi} \right)^{3-2n+2} \right] \delta_{m0} \right.$$
$$\left. - \frac{4}{d^2} \mathrm{i}^m \sum_p \left(\frac{k}{Q_p} \right)^3 \frac{J_{m+3}(Q_p \xi)}{Q_p^2 - k^2} e^{\mathrm{i}m\theta_p} \right), \tag{A.6}$$

and

$$S_m^{\mathrm{K,A}}(k,\boldsymbol{\kappa}) = \frac{1}{I_{m+3}(k\xi)}\left(\left[K_3(k\xi) - \frac{8}{(k\xi)^3} + \frac{1}{k\xi} - \frac{k\xi}{8}\right]\delta_{m0} + \frac{2\pi}{d^2}\mathrm{i}^m \sum_p \left(\frac{k}{Q_p}\right)^3 \frac{J_{m+3}(Q_p\,\xi)e^{\mathrm{i}m\theta_p}}{Q_p^2 + k^2}\right), \tag{A.7}$$

where δ_{mn} is the Kronecker delta, $\theta_p = \arg \mathbf{Q}_p$, $\mathbf{Q}_p = (\kappa_x + 2\pi n/d, \kappa_y + 2\pi m/d)$, $Q_p = \|\mathbf{Q}_p\|_2$, and the vector $\boldsymbol{\xi}$, with corresponding norm ξ, represents an arbitrary vector positioned inside the first Brillouin zone, whose norm is less than unity. Here we have used an acceleration parameter of 3, which is within the recommended range specified in Movchan *et al.* (**9**).

The lattice sum expressions above are valid for square arrays and $m \geq 0$, and so for $m < 0$ one can use the identities $S_{-m}^{\mathrm{Y,A}}(k,\boldsymbol{\kappa}) = \left[S_m^{\mathrm{Y,A}}(k,\boldsymbol{\kappa})\right]^*$ and $S_{-m}^{\mathrm{K,A}}(k,\boldsymbol{\kappa}) = (-1)^m\left[S_m^{\mathrm{K,A}}(k,\boldsymbol{\kappa})\right]^*$, as outlined in (**49**).

Substituting the dynamic Rayleigh identities (A.4) into the system above allows us to obtain

$$\sum_{l=-\infty}^{\infty}\left[(-1)^{l-n}S_{l-n}^{\mathrm{H,A}}J_n(ka) + \delta_{ln}H_n^{(1)}(ka)\right]E_l + \sum_{l=-\infty}^{\infty}\left[(-1)^l S_{l-n}^{\mathrm{K,A}}I_n(ka) + \delta_{ln}K_n(ka)\right]F_l = 0, \tag{A.8}$$

and

$$\sum_{l=-\infty}^{\infty}\left[(-1)^{l-n}S_{l-n}^{\mathrm{H,A}}J_n'(ka) + \delta_{ln}H_n^{(1)\prime}(ka)\right]E_l + \sum_{l=-\infty}^{\infty}\left[(-1)^l S_{l-n}^{\mathrm{K,A}}I_n'(ka) + \delta_{ln}K_n'(ka)\right]F_l = 0, \tag{A.9}$$

which can be solved after suitable truncation at $l = \pm N$ and $n = \pm N$, admitting the block-matrix system

$$\mathbf{A}(k,\boldsymbol{\kappa})\begin{pmatrix}\mathbf{E}\\ \mathbf{F}\end{pmatrix} = 0. \tag{A.10}$$

Here $\mathbf{E}$ and $\mathbf{F}$ represent vectors containing the unknown E_l and F_l coefficients and $\mathbf{A}$ is a block matrix of dimension $(4N+2)\times(4N+2)$. To construct the band surface we search for values of k such that $\det(\mathbf{A}) = 0$, for fixed $\boldsymbol{\kappa}$.